Assessing Modeled Mesoscale Stirring Using Microscale Observations

D. A. CHERIAN,[a] Y. GUO,[b] AND F. O. BRYAN[a]

[a] *NSF National Center for Atmospheric Research, Boulder, Colorado*
[b] *Yale University, New Haven, Connecticut*

ABSTRACT: We assess the representation of mesoscale stirring in a suite of models against an estimate derived from microstructure data collected during the North Atlantic Tracer Release Experiment (NATRE). We draw heavily from the approximate temperature variance budget framework of Ferrari and Polzin. This framework assumes two sources of temperature variance away from boundaries: first, the vertical stirring of the large-scale mean vertical gradient by small-scale turbulence; and second, the lateral stirring of large-scale mean along-isopycnal gradients by mesoscale eddies. Temperature variance so produced is transformed and on average transferred down scales for ultimate dissipation at the microscale at a rate χ estimated using microstructure observations. Ocean models represent these pathways by a vertical mixing parameterization, and an along-isopycnal lateral mixing parameterization (if needed). We assess the rate of variance production by the latter as a residual from the NATRE dataset and compare against the parameterized representations in a suite of model simulations. We find that variance production due to lateral stirring in a Parallel Ocean Program version 2 (POP2) 1/10° simulation agrees well, to within the estimated error bars, with that inferred from the NATRE estimate. A POP2 1° simulation and the Estimating the Circulation and Climate of the Ocean Version 4 release 4 (ECCOV4r4) simulation appear to dissipate an order of magnitude too much variance by applying a lateral diffusivity, when compared to the NATRE estimate, particularly below 1250 m. The ECCOV4r4-adjusted lateral diffusivities are elevated where the microstructure suggests elevated χ sourced from mesoscale stirring. Such elevated values are absent in other diffusivity estimates suggesting the possibility of compensating errors and caution in interpreting ECCOV4r4's adjusted lateral diffusivities.

SIGNIFICANCE STATEMENT: We look at whether microstructure turbulence observations can provide a useful metric for judging the fidelity of representation of mesoscale stirring in a suite of models. We focus on the region of the North Atlantic Tracer Release Experiment (NATRE), the site of a major ocean turbulence observation campaign, and use an approximate variance budget framework for the region with observational estimates from Ferrari and Polzin (2005). The approach provides a novel framework to evaluate the approximate representation of mesoscale stirring in a variety of models.

KEYWORDS: Diapycnal mixing; Turbulence; Isopycnal mixing; General circulation models; Ocean models; Primitive equations model

---

1. Introduction

Ocean tracers weakly diffuse across isopycnal surfaces, approximately surfaces of neutral density, away from boundaries. Global estimates of an appropriate "diapycnal" diffusivity K_d are approximately 10^{-5} m^2 s^{-1} (Whalen et al. 2015; Munk 1966; Kunze 2017; Waterhouse et al. 2014), and the mixing is largely attributed to breaking internal waves (Gregg et al. 1996; MacKinnon et al. 2017). Investigators have inferred significant geographic variations in K_d that appear linked to bottom topography (Kunze et al. 2006) and wind patterns (Whalen et al. 2018; Alford et al. 2016). Where large-scale T or S gradients exist *along* isopycnal surfaces ("spiciness"), they can be efficiently stirred by the ocean's mesoscale to form very sharp gradients, visible as along-isopycnal scatter on a T–S diagram, that are then destroyed by molecular diffusion (e.g., Smith and Ferrari

2009). For example, isopycnal maps of salinity S show the salty Mediterranean outflow spreading westward and southward through the northwest Atlantic at depths between approximately 800 and 1500 m (Fig. 1a). Enhanced middepth T–S scatter is visible in the σ_2 = 36–36.8 kg m^{-3} range (Fig. 2) in Argo profiles collected at the location of the North Atlantic Tracer Release Experiment (NATRE; Ledwell et al. 1998; St. Laurent and Schmitt 1999; black box in Fig. 1). This along-isopycnal salinity gradient is *compensated* by an approximately equivalent along-isopycnal temperature T gradient such that $\alpha\nabla_\rho T = \beta\nabla_\rho S$, where α is the thermal expansion coefficient, β is the haline contraction coefficient, and ∇_ρ is the gradient evaluated on isopycnal surfaces. Lateral stirring and eventual mixing are one explanation for observations of compensated T–S fronts in the thermocline (e.g., Ferrari and Rudnick 2000), the other being double diffusion. Along-isopycnal surface diffusivities K_e are quite large, relative to K_d, with values in the range 500–3000 m^2 s^{-1} (R. Abernathey et al. 2022a). Accurate representation of along-isopycnal stirring is necessary for accurate simulation of ocean tracers, including temperature and salinity, for climate simulations (Griffies et al. 1998). Uncertainties in the value of K_e are consequential for the simulation of anthropogenic
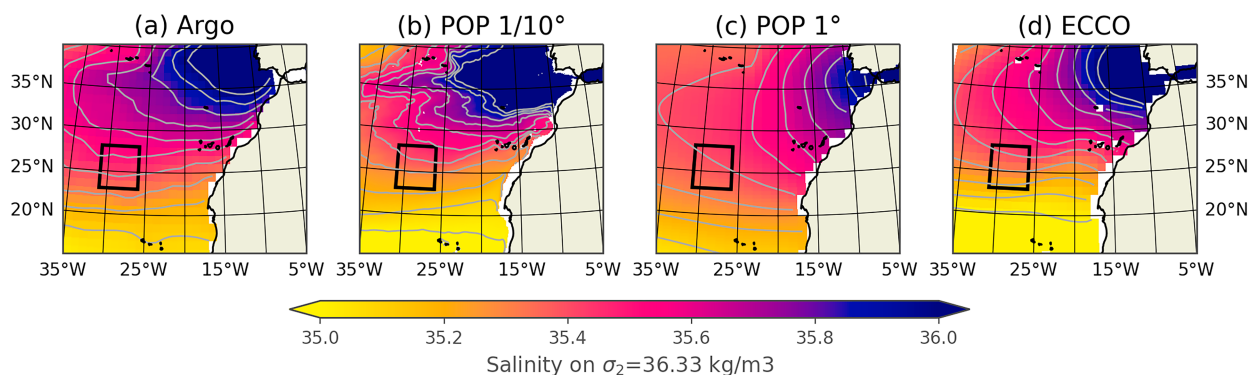

FIG. 1. Time-mean salinity on the $\sigma_2 = 36.33$ kg m^{-3} surface averaged between years 2000 and 2017. The salinity gradient on an isopycnal must be compensated by an approximately equivalent temperature gradient. (a) The Argo climatology (2005–19), (b) POP 1/10° simulation, (c) POP 1° simulation, and (d) the ECCO state estimate. Black box marks the location of the NATRE.

heat uptake, El Niño, and the oxygen field in a coupled model (Gnanadesikan et al. 2015a,b, 2013).

One way to frame the relationship between stirring and dissipation is through a budget for the tracer variance, e.g., T^2. Such a budget expresses a relationship between the rate of variance production, through surface fluxes and stirring of larger-scale gradients by smaller-scale eddies (both mesoscale and microscale turbulence), and the rate of variance dissipation by molecular diffusion (χ; section 2a). When integrated over the global ocean and *assuming* equilibrium statistics, fluid flow must transfer variance from the scales at which variance is generated to the molecular scales at which variance is dissipated, and the rates of generation, transformation, and dissipation must match. Oceanic models cannot resolve fluid flow down to molecular scales and must approximately represent the

transformation of variance using parameterizations that model the variance production term using an "eddy diffusivity" concept. Along-isopycnal stirring is commonly represented by an along-isopycnal diffusivity (Redi 1982), and diapycnal or approximately vertical stirring is represented by a vertical mixing scheme (Large et al. 1994; Jackson et al. 2008; Reichl and Hallberg 2018; Umlauf and Burchard 2003). Observational estimates of these diffusivities, both K_e and K_d, have been derived using many techniques. Here, we work with ocean microstructure observations that can be used to infer K_d from an estimate of the rate of dissipation of temperature variance χ or the rate of kinetic energy dissipation ϵ (Osborn and Cox 1972; Gargett 1989; Gregg 1987; Osborn 1980). Microstructure χ estimates are inferred from observations of the last stages of temperature variance transformation in the ocean. Assuming equilibrium and fidelity, these χ estimates must be related to stirring processes that are parameterized in ocean models. In this paper, we explore interpreting variance pathways and associated parameterizations in a few models, both mesoscale-permitting and mesoscale-parameterizing, in relation to a microstructure dataset collected during the NATRE (Ledwell et al. 1998; St. Laurent and Schmitt 1999), drawing heavily on the analysis by Ferrari and Polzin (2005).

2. Framework

a. Tracer variance pathways

We use the analytical framework of Ferrari and Polzin (2005) and Garrett (2001). Davis (1994a,b) presents a rigorous assessment of the assumptions and approximations used in this framework. Begin with a triple decomposition of the temperature fields

$$T = T_m + T_e + T_t, \tag{1}$$

where the subscripts m, e, and t are loosely identified with the "mean," "mesoscale eddy," and "turbulence" scales. Here, the mean represents the basin-scale gradients over thousands of kilometers similar to the isopycnal salt gradient in Fig. 1a. Turbulence represents the scales of 10 m and smaller, including breaking internal waves and small-scale turbulent eddies. The intermediate-scale contains everything in between mean and turbulence, that
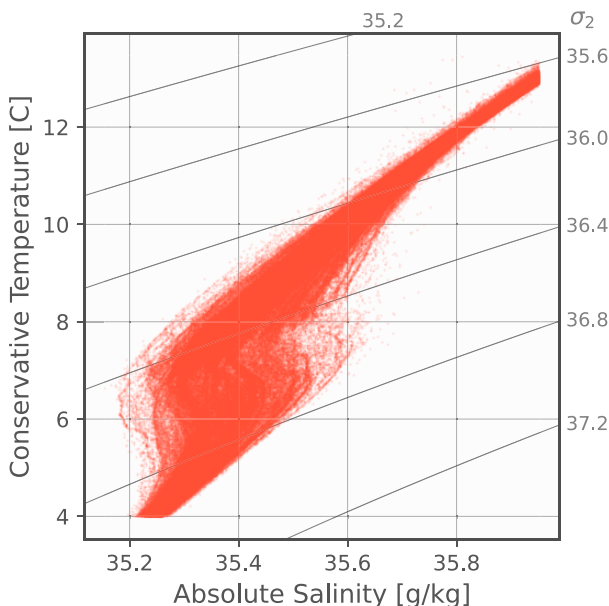

FIG. 2. Conservative Temperature–Absolute Salinity diagram constructed using Argo profiles in the NATRE region (black box in Fig. 1).

is scales between a hundred kilometers and a few meters, including mesoscale eddies and larger-scale internal waves.

We define a "large-scale averaging operator" $\langle \rangle$ that filters out the "eddy" and turbulence scales so that $\langle T \rangle = T_m$ and an intermediate-scale averaging operator $\tilde{}$ that filters out the turbulence scales so that $\tilde{T} = T_m + T_e$. Using such filters assumes a neat separation of the three scales: mean, eddy, and turbulence. It is not evident that such a clear separation exists in the real ocean (Davis 1994b). However, this assumption allows us to make progress toward defining an approximate variance budget framework that allows us to interpret both microstructure observations and numerical simulations in the same context. Ferrari and Polzin (2005) derive the complete variance budget equations for $\langle T_e^2 \rangle$ and $\langle T_t^2 \rangle$ [their Eqs. (4.4) and (4.5)]:

$$\frac{1}{2}(\partial_t + \mathbf{u}_m \cdot \nabla)\langle T_e^2 \rangle + \nabla \cdot \left(\frac{1}{2}\langle \mathbf{u}_e T_e^2 \rangle + \langle \widetilde{\mathbf{u}_t T_t} T_e \rangle - \kappa_T \langle T_e \nabla T_e \rangle \right)$$
$$+ \langle \mathbf{u}_e T_e \rangle \cdot \nabla T_m - \langle \widetilde{\mathbf{u}_t T_t} \cdot \nabla T_e \rangle = -\kappa_T \langle |\nabla T_e|^2 \rangle, \qquad (2)$$

$$\frac{1}{2}(\partial_t + \mathbf{u}_m \cdot \nabla)\langle T_t^2 \rangle + \nabla \cdot \left(\frac{1}{2}\langle \mathbf{u}_t T_t^2 \rangle + \langle \mathbf{u}_e \widetilde{T_t^2} \rangle - \kappa_T \langle T_t \nabla T_t \rangle \right)$$
$$+ \langle \widetilde{\mathbf{u}_t T_t} \cdot \nabla (T_m + T_e) \rangle = -\kappa_T \langle |\nabla T_t|^2 \rangle. \qquad (3)$$

Here, $\mathbf{u}$ represents the three-dimensional velocity vector, ∇ represents the full three-dimensional gradient operator, and κ_T is the molecular diffusivity of temperature. Assuming stationarity, we can drop the time derivative term in both equations. Davis (1994a) examined these assumptions in quite some detail and concluded that the assumption of stationarity is reasonable outside of regions of strong upwelling and away from boundaries (that is external sources or sinks). Assuming homogeneity allows us to drop the advection term. We a priori assume that the divergence of turbulent and eddy fluxes of variance (also known as the triple product terms, e.g., $\langle \mathbf{u}_e T_e^2 \rangle$) can be ignored. We follow Ferrari and Polzin (2005) in making this assumption regardless and treat the resulting analysis as an evaluation of consistency between models and observations within this *approximate* framework.

The last term of (2), the molecular dissipation of mesoscale gradients, is ignored since mesoscale gradients are relatively weak. Under these assumptions, the approximate mesoscale and turbulent temperature variance budgets are as follows:

$$\langle \mathbf{u}_e T_e \rangle \cdot \nabla T_m - \langle \widetilde{\mathbf{u}_t T_t} \cdot \nabla T_e \rangle \approx 0, \qquad (4)$$

$$\langle \widetilde{\mathbf{u}_t T_t} \cdot \nabla (T_m + T_e) \rangle \approx -\frac{1}{2} \langle \tilde{\chi} \rangle; \quad \chi = 2\kappa_T |\nabla T_t|^2. \qquad (5)$$

Here, χ represents the instantaneous rate of dissipation of temperature variance at the molecular scale.

Equation (4), derived from that for mesoscale variance $\langle T_e^2 \rangle$, states that the mesoscale field generates variance by the stirring of the mean and this variance cascades down to the microscale turbulence through the "scale transformation term" $\chi_e \equiv \langle \widetilde{\mathbf{u}_t T_t} \cdot \nabla T_e \rangle$. Equation (5), derived from that for microscale variance $\langle T_t^2 \rangle$, states that the microscale turbulence stirs the combination of the mean and eddy fields $(T_m + T_e)$ to generate variance that is eventually dissipated at the molecular

scale at the rate χ. The scale transformation term χ_e is of opposite sign in the two equations highlighting its role in linking the mesoscale and microscale. Garrett (2001) presented an illustrative summary of these pathways (Fig. 3a).

Adding (4) and (5) yields the approximate balance,

$$\langle \widetilde{\mathbf{u}_t T_t} \rangle \cdot \nabla T_m + \underbrace{\langle \widetilde{\mathbf{u}_e T_e} \rangle \cdot \nabla T_m}_{\chi_e} \approx -\frac{1}{2} \langle \chi \rangle, \qquad (6)$$

that is the variance dissipated at the molecular scale is approximately generated by the stirring of the mean field T_m by the mesoscale and microscale turbulence. While $\langle \tilde{a} \rangle = \langle a \rangle$, we preserve $\tilde{}$ in (6) for clarity.

b. Variance pathways as a model diagnostic

Following Alford et al. (2005), we can further simplify (6) assuming (i) that $\mathbf{u}_t$ is isotropic and $\partial_z T_m \gg \nabla^h T_m$, so $\langle \widetilde{\mathbf{u}_t T_t} \rangle \cdot \nabla T_m \approx \langle \widetilde{w_t T_t} \rangle \cdot \partial_z T_m$; and (ii) that mesoscale motions stir the along-isopycnal horizontal gradient $\nabla^h_\rho T_m$, so that $\chi_e \approx \langle \widetilde{\mathbf{u}_e^h T_e} \rangle \cdot \nabla^h_\rho T_m$ (superscript h represents the horizontal components) yielding

$$\langle \widetilde{w_t T_t} \rangle \cdot \partial_z T_m + \underbrace{\langle \widetilde{\mathbf{u}_e^h T_e} \rangle \cdot \nabla^h_\rho T_m}_{\chi_e} \approx -\frac{1}{2} \langle \chi \rangle. \qquad (7)$$

In a mesoscale-resolving model, the second term is resolved and we can qualitatively identify the turbulence as representing subgrid-scale motions whose effect on the mean scales is parameterized using both a vertical mixing scheme and a lateral diffusion scheme (section 4b). For coarser models where even the mesoscale is parameterized, χ_e is commonly modeled using an along-isopycnal Redi (1982) diffusivity (section 5b). The assignment of scales here is qualitative and only influences the interpretation in what follows. For example, Alford et al. (2005) derives (7) as a framework for interpreting observations of a 1-km scale lateral thermohaline intrusion. Our analysis is concerned with χ_e, estimated as a residual from microstructure observations [difference between the rhs and the first term on the lhs of (7)], or more directly from numerical simulations, and other mesoscale eddy diffusivity estimates.

A large number of approximations are required to get to this point, namely, those of homogeneity, stationarity, a priori ignoring of the triple correlation term, and an assumption that we are working in a region away from external sources and sinks of variance. However, this framework has value in qualitatively describing the nature of variance cascades in the ocean (Garrett 2001; Ferrari and Polzin 2005; Spingys et al. 2021; Naveira Garabato et al. 2016). Specifically, Ferrari and Polzin (2005), Spingys et al. (2021), and Naveira Garabato et al. (2016) estimate the rhs term $\langle \chi \rangle /2$ and the first term on the lhs $\langle \widetilde{w_t T_t} \rangle \cdot \partial_z T_m$ using in situ microstructure data. The difference between the two terms, where statistically significant, is then interpreted as a sign of variance production by mesoscale eddy stirring, as we do below. Later, Smith and Ferrari (2009) used a 1-km quasigeostrophic model initialized with climatological fields, averaged over the NATRE region, to explicitly diagnose the eddy stirring term and find evidence for a

$$\chi_e = \langle \widetilde{u_e^h T_e} \rangle \cdot \nabla_\rho^h T_m$$

mesoscale

$$\chi_e \cong \langle \widetilde{u_t T_t} \cdot \nabla T_e \rangle$$

mean

$$\langle \widetilde{w_t T_t} \rangle \cdot \partial_z T_m$$

microscale $\dfrac{\langle \chi \rangle}{2}$

(a) Hypothesis (Garrett et al., 2001)

mesoscale

mean

Assume residual

$$-K_\rho^m (\partial_z T_m)^2$$

microscale $\dfrac{\langle \chi \rangle}{2}$

(b) NATRE (Ferrari & Polzin, 2005)

mesoscale $-\langle T_e A_h \nabla^4 T_e \rangle$

biharmonic lateral diffusivity

mean

microscale $\dfrac{\langle \chi \rangle}{2}$

$$K_T (\partial_z T_m)^2 \quad \langle T_e \partial_z (K_T \partial_z T_e) \rangle$$

KPP

(c) POP 1/10° (Guo et al. 2022)

mesoscale

$$\chi_e = K_e |\nabla_\rho^h T|^2 \text{ Along-isopycnal/}$$
Redi diffusivity

mean

microscale $\dfrac{\langle \chi \rangle}{2}$

$$-K_T (\partial_z T)^2$$
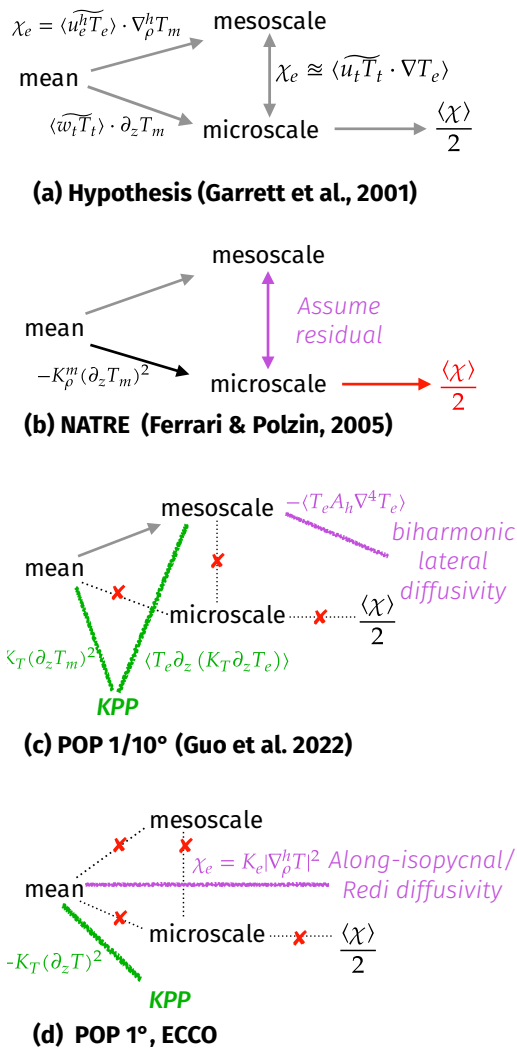
KPP

(d) POP 1°, ECCO

FIG. 3. Schematic of approximate tracer variance pathways. Red crosses over dashed lines mark unresolved pathways that are parameterized. Colors match terms presented in Fig. 4. (a) Hypothesis from Garrett (2001). (b) Analysis framework of Ferrari and Polzin (2005) based on (a), but with colors matching terms in Fig. 4a. (c) For POP 1/10° simulation. The model resolves the mean → mesoscale pathway but the rest is parameterized through either KPP vertical mixing or biharmonic lateral diffusion. Terms from Guo et al. (2022) are rewritten in our notation. (d) For the POP 1° and ECCO simulations. These do not resolve the mesoscale, so all pathways are parameterized.

similar balance in that model. Guo et al. (2022) also found an approximate three-term balance reminiscent of (6) in most parts of the ocean as simulated by a 1/10° Community Earth System Model-Parallel Ocean Program version 2 (CESM-POP2) configuration, again suggesting that (6) is an approximate framework with qualitative value.

c. Objectives

The central question of this paper is whether the estimated mesoscale stirring term in a mesoscale-resolving model and the

parameterized variance dissipated by Redi (1982) diffusion in coarser models compare well against the estimated magnitude of the scale transformation term using the NATRE observations and the Ferrari and Polzin (2005) methodology. We compare resolved and parameterized mesoscale eddy stirring to an observational estimate using the variance production rate χ_e as a metric. This rate is a direct output of the lateral diffusivity scheme, so the comparison is *direct* in the sense of Large and Gent (1999). We choose χ_e as our metric instead of an eddy diffusivity K_e to avoid further uncertainties associated with defining the mean gradient $\nabla_\rho^h T_m$ (see also Alford et al. 2005), and because χ is the fundamental turbulence quantity inferred from a microstructure measurement. This choice, however, means that errors in simulating the mean field T_m affect the interpretation of our metric χ_e (section 5).

The analysis presented here is novel in that it compares realistic primitive equation ocean models used in climate projection and prediction configurations with realistic forcing to microstructure-based inferences about variance pathways in the ocean. In this way, it differs from the work of Smith and Ferrari (2009) who used a 1-km quasigeostrophic model to support the interpretation that mesoscale eddy stirring is the major contributor to the scale transformation term in the NATRE region.

3. Datasets

a. NATRE microstructure dataset

The core microstructure dataset used in this analysis is that from the NATRE (Ledwell et al. 1998; St. Laurent and Schmitt 1999), collected in April 1992 using the Woods Hole Oceanographic Institution High Resolution Profiler (HRP; Schmit et al. 1988). We use vertical profiles from the "large scale survey": approximately 100 profiles down to 2000 dbar collected in a 400 km × 400 km box (24°–28°N; 26.5°–31°W) as a 10 × 10 grid at approximately 0.5° (44.4 km) spacing. These profiles contain quality-controlled estimates of temperature, salinity, dissipation rate of temperature variance χ, and dissipation rate of turbulence kinetic energy ϵ at 0.5-dbar spacing. The dataset is available publicly in the National Science Foundation microstructure database[1] (Waterhouse et al. 2014).

b. Observational estimates of K_e

We use two observational estimates of K_e, both of which use mixing length theory to express diffusivity as

$$K_e \sim C U_e L_e, \tag{8}$$

where C is a constant, U_e is an appropriate velocity scale, and L_e is a length scale. The first estimate, from Cole et al. (2015), uses a root-mean-square velocity $\mathbf{u}_{\text{rms}} = \sqrt{\langle u'^2 + v'^2 \rangle}$ from the ECCO2 state estimate (Menemenlis et al. 2008) for U_e. They estimate a mixing length scale L_e using salinity anomalies on isopycnal surfaces,

---

[1] https://microstructure.ucsd.edu.

$$L_e = \frac{\sqrt{\langle S'S' \rangle}}{\langle |\nabla S| \rangle}. \tag{9}$$

Primed quantities are defined as the anomaly relative to a 1-yr running average of that quantity q, so $q' = q - \overline{q}$. Salinity on an isopycnal surface S is estimated using the mapped Argo climatology of Roemmich and Gilson (2009). The constant C is chosen to be 0.16 (Wunsch 1999; Klocker and Abernathey 2014). These estimates are publicly available (Cole et al. 2018).

Groeskamp et al. (2020b) estimate K_e by specifying U_e as the root-mean-square of the geostrophic velocity $\mathbf{u}_{rms} = \sqrt{2\,EKE_0}$, where EKE_0 is the surface geostrophic eddy kinetic energy estimated from sea surface height and L_e is the first Rossby radius of deformation calculated as the eigenvalue associated with the first surface mode (LaCasce and Groeskamp 2020). In addition, they account for a depth dependence of K_e that models the suppression of eddy stirring in the presence of a mean flow (Klocker et al. 2012; Ferrari and Nikurashin 2010). Depth dependence arises from the depth dependence of the mean flow $U(z)$ and depth dependence of the eddy velocity scale $\mathbf{u}_{rms}(z)$. The vertical structure of $\mathbf{u}_{rms}$ is determined by extrapolating the surface EKE downward using a vertical mode structure estimated using the "first surface mode" (de La Lama et al. 2016; LaCasce 2017). See Groeskamp et al. (2020b) for more details. These estimates of K_e are also publicly available (Groeskamp et al. 2020a).

c. Simulations

We interpret the fidelity of the mesoscale stirring representation in a suite of global model integrations described below, using the NATRE observations.

1) CESM-H POP 1/10°

Guo et al. (2022) present a closed temperature variance budget analysis for an interannually forced simulation using the Parallel Ocean Program version 2 (POP2; Smith et al. 2010) component of the Community Earth System Model version 2 (CESM2; Danabasoglu et al. 2020) with a grid of nominal 1/10° horizontal spacing and 62 vertical levels (termed CESM-H). In the NATRE region, the vertical grid spacing is 90–155 m between depths of 800 and 1500 m. The model configuration is similar to that of Bryan and Bachman (2015) but is instead forced using the Japanese 55-yr Reanalysis (JRA55) dataset (Tsujino et al. 2018). This simulation uses the K-profile parameterization (KPP) scheme (Large et al. 1994) to parameterize vertical mixing and biharmonic viscosity and diffusivity to represent subgrid-scale horizontal stirring and eventual mixing. Biharmonic viscosity and diffusivity values vary with the cube of the grid spacing and have equatorial values of 2.7×10^{10} and 3×10^9 m^4 s^{-1}, respectively. This simulation simulates the salinity field associated with the Mediterranean outflow with reasonable fidelity (Fig. 1b).

2) CESM-L POP 1°

We diagnose the spinup of a lower-resolution simulation, termed CESM-L, using the CESM2 (Danabasoglu et al. 2020)

ocean component z-coordinate model POP2 (Smith et al. 2010) at a nominal spacing of 1° and 60 vertical levels with a spacing of 90–155 m between depths of 800 and 1500 m (same as the previously described CESM-H simulation). This simulation is initialized with the *World Ocean Atlas 2018* (Boyer et al. 2018) temperature and salinity fields and zero velocities following the Ocean Model Intercomparison Project (OMIP) protocol (Griffies et al. 2016). The simulation is integrated forwards for six cycles or repeats of the JRA55 surface forcing (Tsujino et al. 2018).

This simulation does not resolve mesoscale eddies and relies on an isopycnal Redi diffusivity applied using the discretization of Griffies et al. (1998) to model along-isopycnal eddy stirring, variance generation, and eventual dissipation. The isopycnal diffusivity formulation is identical to that in CESM1 (Danabasoglu et al. 2012), with the exception of increased values at depth [600 m^2 s^{-1} instead of 300 m^2 s^{-1} in CESM1 (Danabasoglu et al. 2020)]. The diffusivity can be as large as 3000 m^2 s^{-1} near the surface and decreases with depth as a function of buoyancy frequency N (Danabasoglu and Marshall 2007) with a minimum value of 600 m^2 s^{-1} at depths deeper than approximately 2000 m. No other lateral diffusivity is applied. This simulation uses the KPP scheme (Large et al. 1994) to parameterize vertical mixing.

3) ECCOv4R4

The ECCO project provides a dynamically consistent global ocean state estimate for the 1992–2011 period, constrained using a number of remote sensing and in situ datasets (Forget et al. 2015a). This configuration uses a grid with approximately 1° horizontal spacing at the equator and 50 vertical levels with grid spacings of approximately 100 m in the NATRE region in the 800–1500-dbar range. A highlight of version 4 is that the time-invariant three-dimensional fields of diapycnal diffusivity, isopycnal Redi diffusivity K_e, and the Gent et al. (1995) coefficient are adjusted subject to the data constraints provided, starting from constant first guesses of 10^{-5}, 10^{-3}, and 10^3 m^2 s^{-1}, respectively. These adjustments significantly improve the representation of the mean state, reduce model drift, and are mostly sensitive to the constraints provided by the Argo dataset (Forget et al. 2015b).

4. Results: Microstructure and mesoscale-resolving simulations

a. Microstructure estimate: NATRE

For the NATRE region, Ferrari and Polzin (2005) estimate the first term in (7) $\langle \widetilde{w_t T_t} \rangle \cdot \partial_z T_m$ as well as the rhs $\langle \chi \rangle / 2$ using the NATRE microstructure data (T, S, ϵ, χ). They find significant differences between the two terms between 800 and 1500 dbar and interpret the differences as a sign of variance generation by mesoscale stirring (Fig. 4a). They define $\langle \rangle$ as a horizontal average over the entire 400 km × 400 km box, a vertical average over approximately 100 m, and a time average over approximately 18 days. Averages of all quantities are computed in neutral density bins whose mean depths estimated using the data are approximately 100 m apart.
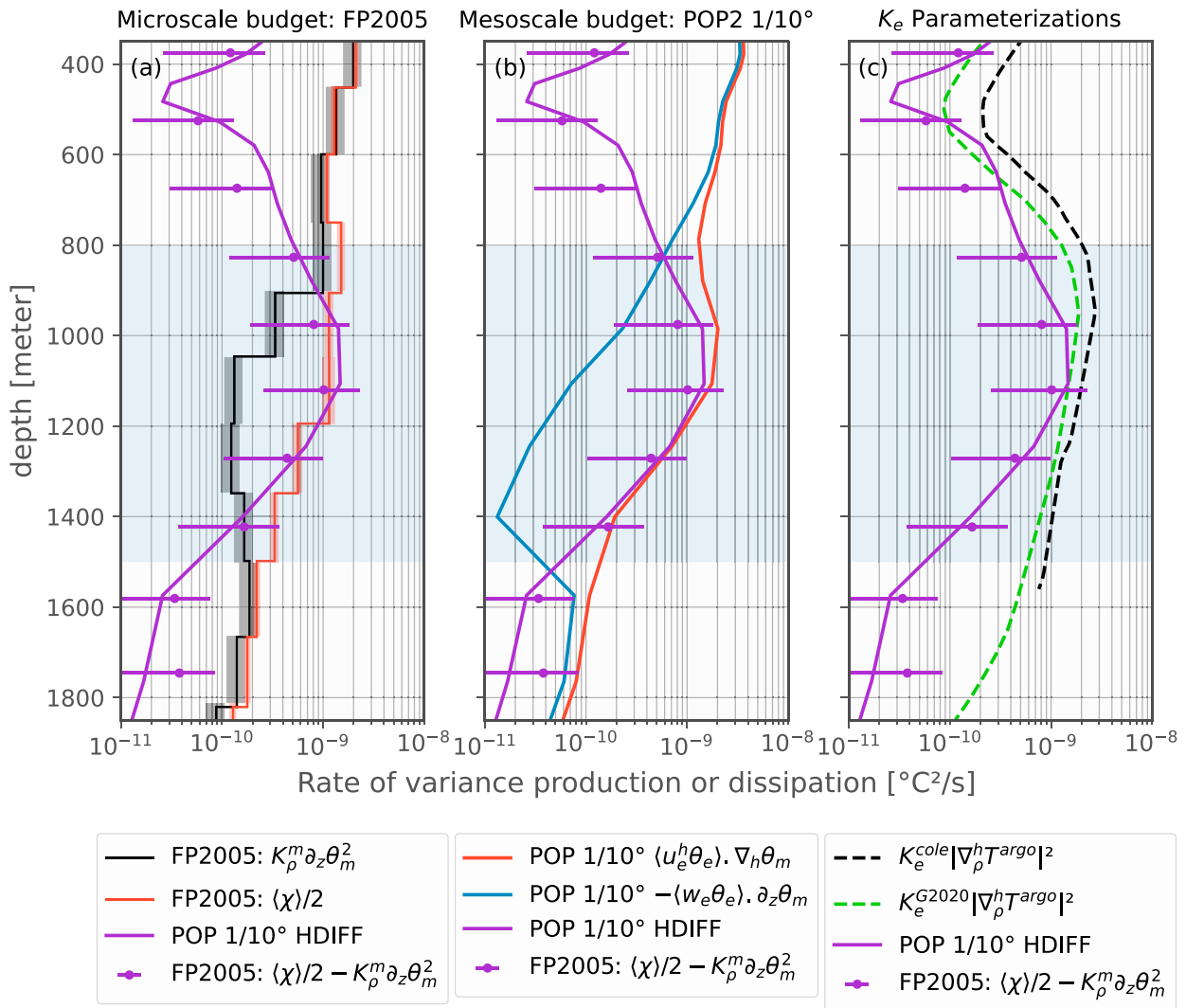
FIG. 4. Mesoscale and microscale variance production and dissipation terms averaged along density surfaces over the NATRE region (Fig. 1) for a variety of datasets. The 800–1500-m depth range is highlighted. (a) NATRE microscale variance budget presented by Ferrari and Polzin (2005) (red, black, labeled FP2005). The χ_e estimated as residual using the NATRE data (purple bars) agrees quite well with χ_e from CESM-H POP2 1/10° simulation (solid purple; Guo et al. 2022). (b) Mesoscale variance budget terms from Guo et al. (2022) illustrating an approximate three-term balance between lateral stirring (red), vertical stirring (blue), and lateral dissipation χ_e (purple). (c) The χ_e estimates using the K_e estimates of Groeskamp et al. (2020b) and Cole et al. (2015) and $\nabla_\rho^h T$ estimated using the Argo mapped climatology (section 4a), compared to that from NATRE and Guo et al. (2022).

They assume that buoyancy b over the $O(100)$ m vertical scale is dominated by temperature so that vertical diffusivities of T and b are equal on a 100-m scale: $K_T^m \approx K_\rho^m$. Then,

$$\langle w_t T_t \rangle = -K_T^m (\partial_z T_m) \approx -K_\rho^m (\partial_z T_m). \qquad (10)$$

Osborn (1980) relates K_ρ to the average rate of dissipation of turbulent kinetic energy ϵ:

$$K_\rho^m = \Gamma \frac{\langle \epsilon \rangle}{\partial_z b_m}, \qquad (11)$$

with the flux coefficient Γ assumed to be 0.2, consistent with recommend practice (Gregg et al. 2018). They estimate mean

vertical gradient $\partial_z T_m$ using a $O(100)$ m linear fit along the vertical axis to T measurements in each neutral density bin.

We are able to reproduce their Fig. 10 in our Fig. 4a. We choose to use potential temperature and practical salinity, so that we can reproduce the usage of a neutral density variable by Ferrari and Polzin (2005) and ensure that our results are directly comparable. Between approximately 800 and 1500 m (highlighted), the rate of variance dissipation $\langle \chi \rangle / 2$ exceeds the variance produced by microscale stirring of the mean $K_\rho^m \partial_z T_m^2$ suggesting the presence of another variance source. The residual between these two terms is marked by purple bars in all panels, where the width of the bars represents the error estimates computed following the procedure outlined in

the appendix of Ferrari and Polzin (2005). This depth range is the location of a large water mass contrast along isopycnals. Both Ferrari and Polzin (2005) and Smith and Ferrari (2009) argue that mesoscale stirring of the mean gradient along isopycnals accounts for the necessary variance production (Fig. 3b). This inference is supported by the variance budget calculated for a mesoscale-resolving simulation (Guo et al. 2022), as we describe next. For further discussion of the NATRE results, see Ferrari and Polzin (2005) and Smith and Ferrari (2009).

For the remainder of the paper, keep in mind that the microstructure estimate suggests that in the top 2000 m of the NATRE region, mesoscale stirring of the mean is the dominant variance production term between approximately 800 and 1500 m, and microscale stirring of the mean vertical gradient dominates the rest of the water column. We now examine whether numerical simulations reproduce this vertical dependence of the approximate variance budget balance.

b. Diagnosing a mesoscale-resolving simulation: CESM-H POP2 1/10°

Guo et al. (2022) present a variance budget for the mesoscale, see Eq. (7), in a 1/10° POP2 simulation. Their budget is constructed in *depth space* using a "double decomposition" of the *cell-averaged* equations, which makes it a triple decomposition if we identify the turbulence as subgrid-scale motions. In addition, they split the resolved scale stirring, assumed to be primarily mesoscale stirring, of the mean into horizontal and vertical portions. The approximate mesoscale variance budget (4) can be rewritten from

$$\langle \mathbf{u}_e T_e \rangle \cdot \nabla T_m - \langle \widetilde{\mathbf{u}_t T_t} \cdot \nabla T_e \rangle \approx 0 \qquad (12)$$

to

$$\underbrace{\langle \mathbf{u}_e^h T_e \rangle \cdot \nabla^h T_m}_{\text{BC}_T} + \underbrace{\langle w_e T_e \rangle \partial_z T_m}_{\text{PKC}_T} - \underbrace{\langle \widetilde{\mathbf{u}_t T_t} \cdot \nabla T_e \rangle}_{\text{HDIFF+VMIX}} \approx 0. \qquad (13)$$

The term labels in (13) are reproduced from Guo et al. (2022) to allow easy comparison. The BC$_T$ refers to "baroclinic conversion from mean to eddy potential energy" associated with temperature variability, PKC$_T$ refers to a potential–kinetic energy conversion by baroclinic instability, and finally, the dissipation terms due to the vertical mixing scheme and a horizontal biharmonic diffusion are termed VMIX and HDIFF, respectively. This simulation explicitly resolves mesoscale eddies, their stirring of mean gradients along isopycnals, and therefore the mean → mesoscale variance pathway. However, the model is too coarse to convert the horizontal variability to vertical variability to be dissipated by the vertical mixing scheme (Smith and Ferrari 2009), since the vertical spacings are approximately 100–150 m at the depth range of spiciness variability. Instead, the variance generated by mesoscale stirring cascades down to the grid scale where it is removed by gridscale dissipation $\langle \widetilde{\mathbf{u}_t T_t} \cdot \nabla T_e \rangle$, here a combination of KPP vertical mixing and a biharmonic lateral diffusivity (Fig. 3c). These two are the VMIX and HDIFF terms in Guo et al.

(2022). The remaining terms in their budget are negligible in the NATRE region (not shown here). We can identify the scale transformation term $\chi_e = \langle \widetilde{\mathbf{u}_t T_t} \cdot \nabla T_e \rangle$ as the sum of the two dissipative terms in their analysis: VMIX and HDIFF. In the NATRE region, the variance dissipated by the VMIX is more than an order of magnitude smaller than that dissipated by the HDIFF (not shown). In this way, biharmonic diffusivity plays a physical role in representing the variance pathway from the mesoscale → microscale → molecular scale diffusion.

Figure 4b presents the three term balance in (13) from their analysis, horizontally averaged over the 400 km × 400 km NATRE region and time averaged over the years 2000–19. The vertical averaging scale is inherited from the choice of model vertical grid, which has grid spacings of 90–155 m between depths of 800 and 1500 m. These spacings are comparable to the 100-m averaging scale used by Ferrari and Polzin (2005) and in section 4a. In the top 800 m of the water column, spiciness or $|\nabla_\rho^h T|$ is low (shown in Fig. 5b). Here, lateral eddy stirring of T_m generates density anomalies with associated potential energy anomalies ["eddy potential energy" (EPE)]. The EPE is then converted to EKE, so $\langle \mathbf{u}_e^h T_e \rangle \cdot \nabla^h T_m \approx -\langle w_e T_e \rangle \partial_z T_m$ and only a small amount of temperature variance is cascaded down to the grid scale for dissipation. Such energy transfers are parameterized in coarser models using the Gent et al. (1995) scheme. Note that if the budget was constructed in isopycnal space, this balance would not appear.

Between ~800 and 1500 m, spiciness is large. Here, eddy stirring is effective at generating T and S anomalies that are density-compensated and have almost no density or EPE signal. Such compensated variance is cascaded down to the grid scale for dissipation by a lateral diffusivity. So, χ_e balances the horizontal stirring term while the vertical mesoscale stirring term is weak (Fig. 4b).

We can now directly compare χ_e in this simulation to the residual computed using the microstructure estimates (section 4a). We find a *remarkable* agreement between the two in that the simulated variance dissipation is within the error bars of the residual from the observations. Note that the only comparable previous analysis of Smith and Ferrari (2009) used a quasigeostrophic model at 1-km resolution, while Guo et al. (2022) present a closed variance budget for the mesoscale in a realistically forced mesoscale-resolving primitive equation simulation.

5. Results: Diagnosing coarser simulations

Coarse climate models represent the effect of along-isopycnal stirring using a Redi (1982) diffusivity K_e applied along isopycnal surfaces (treated as approximately neutral surfaces). Cole et al. (2015) and Groeskamp et al. (2020b) present observational estimates for isopycnal K_e applicable to such coarse models. With coarser horizontal grid spacings of 1/4° or larger, such models cannot resolve, or at best only partially resolve, the mean → mesoscale pathway. For such models, we estimate χ_e as the variance dissipated by the application of along-isopycnal diffusivity and compare to the microstructure residual (Fig. 3d). Next, we explore whether such a framework yields insight into the
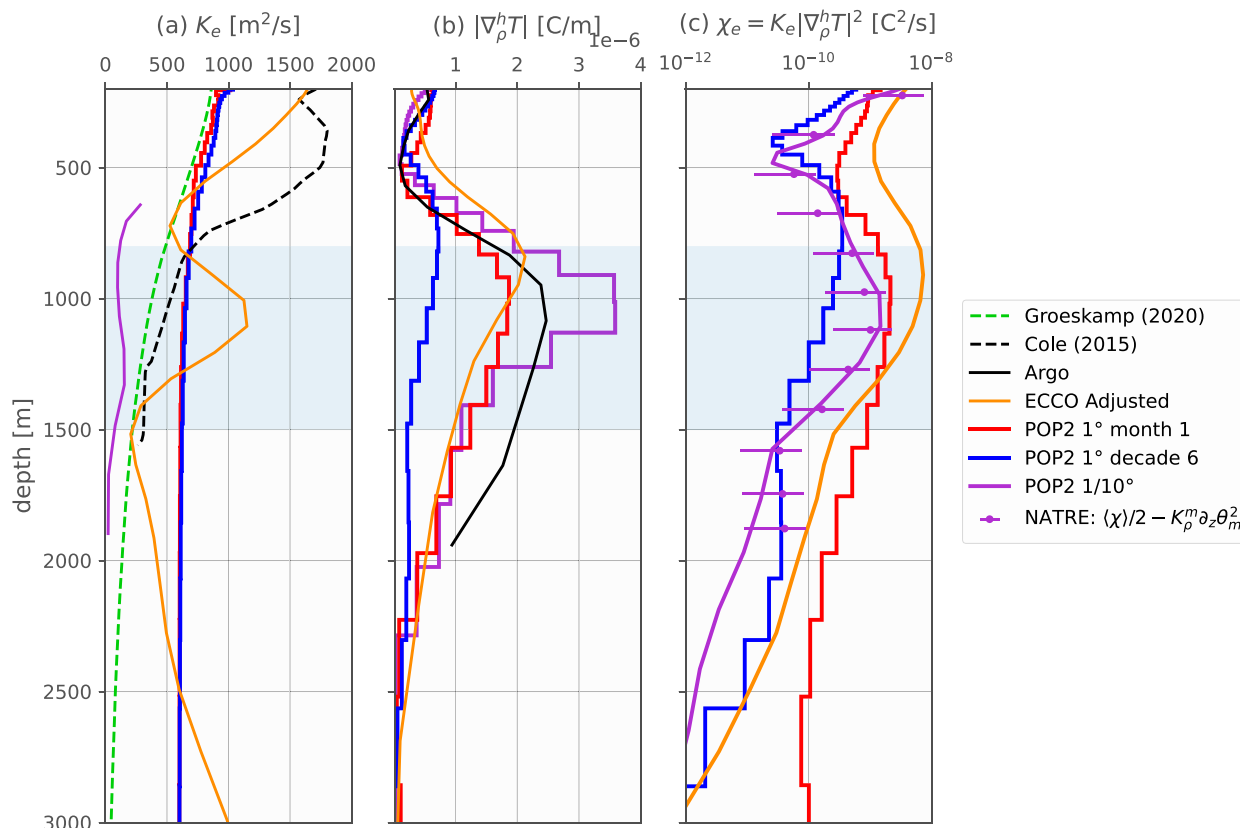
FIG. 5. Diagnosing the spinup of a POP2 1° simulation, and ECCO, in the NATRE region. The 800–1500-m depth range is highlighted. (a) Along-isopycnal diffusivities K_e from the POP2 integration averaged over the first month (red) and the sixth decade of integration (blue) and estimates from Groeskamp et al. (2020b) (green) and Cole et al. (2015) (black dashed). For comparison, we also present an effective diffusivity $\hat{K}_e$ for the POP2 1/10° simulation estimated as $\chi_e/|\nabla_\rho^h T^2|$. All values are averaged over the NATRE region. (b) Along-isopycnal lateral temperature gradient $|\nabla_\rho^h T^2|$ from the Argo climatology (black) and diagnosed using plane fits for the POP2 1° integration and the POP2 1/10° integration. For consistency, the 1/10° fields are regridded to the grid of the 1° simulation before fitting the plane. (c) The χ^e from the POP2 integrations and NATRE.

fidelity of the diffusivity estimates and coarse models. Doing so is complicated by the fact that such models are usually deficient in other areas. A relevant deficiency for this analysis is a lack of fidelity in simulating the Mediterranean outflow (Fig. 1). In variance budget terms, if the model is unable to maintain the along-isopycnal water mass contrast it is initialized with, then it is not going to replicate the right χ_e, even if it applied the right diffusivities.

a. Assessing eddy diffusivity estimates derived from observations

Variance production rate χ_e associated with the mesoscale eddy diffusivity estimates of Cole et al. (2015) and Groeskamp et al. (2020b) is estimated as $K_e|\nabla_\rho^h T_m|^2$. The isopycnal horizontal temperature gradient $\nabla_\rho^h T_m$ is estimated by fitting a plane to the mapped Argo climatology temperature field on an isopycnal surface over the NATRE box, following the approach of Ferrari and Polzin (2005). Figure 4c compares these χ_e estimates to the NATRE residual. While the comparison appears reasonable in the top 1400 m or so, the values below that are approximately

one to two orders of magnitude too high. It is unclear how to interpret the discrepancy given the very significant assumptions that go into both the microstructure estimate and the K_e estimates.

We can also compare these K_e estimates to a crude estimate of the "effective diffusivity" of flow in the NATRE region as simulated by the 1/10° simulation using

$$\hat{K}_e = \frac{\chi_e}{|\nabla_\rho^h T|^2}. \qquad (14)$$

Again, $|\nabla_\rho^h T|$ is estimated by a plane fit to the time-mean T field along an isopycnal surface; and χ_e is averaged in time, interpolated to density space, and then averaged over the NATRE box. Estimates are discarded where $|\nabla_\rho^h T|^2 < 5 \times 10^{-13}$°C^2 m^{-2}. In the 1000–1500-dbar range, effective diffusivity values vary between 100 and 250 m^2 s^{-1} and are approximately a factor of two smaller than the Groeskamp et al. (2020a) estimate (150–400 m^2 s^{-1}). We caution that this $\hat{K}_e$ estimate is quite crude and more sophisticated methods for estimating an effective diffusivity exist (e.g., Bachman et al. 2015, 2020).

b. Diagnosing CESM-L POP2 1° spinup

We diagnose the spin up of the circulation comparing the first month and last decade of the first cycle of forcing. Simulation outputs include the monthly mean Redi diffusivity K_e and T, S fields. We interpolate monthly mean T and K_e to isopycnal surfaces, estimate $|\nabla_\rho^h T|^2$ using plane fits along isopycnals, and then calculate $\chi_e = K_e |\nabla_\rho^h T|^2$ at monthly frequency.

Averaged over the NATRE box for the first month of integration, χ_e compares quite well to the microstructure residual at approximately 1000 dbar (Fig. 5c). Being initialized from observations, the initial along-isopycnal gradients agrees well with observations (Fig. 5b). So, when a relatively accurate along-isopycnal gradient exists, the right amount of variance is dissipated. Deeper down between 1500 and 2000 dbar, $|\nabla_\rho^h T|$ is smaller but not negligible and in reasonable agreement with the Argo climatology (Fig. 5b). Here, χ_e exceeds the NATRE and POP 1/10° χ^e by about a factor of 30 suggesting too high diffusivities K_e (Fig. 5c). This interpretation agrees with the Groeskamp et al. (2020b) and Cole et al. (2015) K_e estimates that show a strong decay with depth by 1500 dbar. As the model is integrated forward, $\nabla_\rho^h T$ continues to decrease and the middepth peak is significantly weaker than the Argo climatology by the end of the first cycle of integration (Fig. 5b).

One possible interpretation is that at least in this region, the model is not overly diffusive at 1000 dbar but instead has a problem maintaining the water mass contrast along isopycnals through the advection of the Mediterranean outflow. This interpretation is supported by the isopycnal salinity maps in Fig. 1c where we see that the along-isopycnal salinity gradient is significantly weaker than that in the observations much closer to the mouth of the Mediterranean (e.g., see 30°N, 20°W). In other words, errors in variance budget at 1000 dbar appear to arise from errors in the simulation of the mean state, rather than from errors in parameterizing the mesoscale in the NATRE region.

Between 1500 and 2000 dbar, the vertical profile of K_e does not decay with depth as quickly as the inferred decay of K_e from observations (Groeskamp et al. 2020b; Cole et al. 2015). These high K_e values appear responsible for too much lateral dissipation in the model below 1500 dbar. However, remember that both the microstructure measurements and the 1/10° model suggest that microscale turbulence is the dominant stirring term at these depths for the temperature variance budget. Thus, inaccuracies in K_e and χ_e are of minor consequence for the model's simulation of the mean *temperature* field, but might be more consequential for other tracers. Indeed, Danabasoglu et al. (2020) mention that enhanced K_e values at depth are used to improve the representation of passive tracers.

c. Interpreting ECCOV4r4 K_e adjustments

The ECCO simulation is of particular interest because it adjusts K_e to reduce misfit to observations (Forget et al. 2015b). The ECCO configuration uses the advective form of the Gent–McWilliams parameterization, and the isopycnal fluxes are calculated using the symmetric Redi tensor (MITgcm Group 2023).

$$\mathbf{K} = K_e \begin{pmatrix} 1 & 0 & S_x \\ 0 & 1 & S_y \\ S_x & S_y & S^2 \end{pmatrix} \equiv \begin{pmatrix} K_{xx} & 0 & K_{xz} \\ 0 & K_{yy} & K_{yz} \\ K_{zx} & K_{zy} & K_{zz} \end{pmatrix},$$

where S_x, S_y, and S_z are the isopycnal slopes.

We reproduce the forward running simulation for ECCO release 4 version 4 following Wang and Fenty (2023) and save monthly averages of the variance dissipation rate χ_e due to isopycnal diffusion. We accumulate χ_e calculated online during model integration using the tensor product $\chi_e \equiv \partial_m T K^{mn} \partial_n T$, so

$$\chi_e = K_{xx}\left(\frac{\partial T}{\partial x}\right)^2 + K_{yy}\left(\frac{\partial T}{\partial y}\right)^2 + K_{zz}\left(\frac{\partial T}{\partial z}\right)^2 + 2K_{xz}\frac{\partial T}{\partial x}\frac{\partial T}{\partial z}$$
$$+ 2K_{yz}\frac{\partial T}{\partial y}\frac{\partial T}{\partial z}. \tag{15}$$

We use the same gradient estimates used by the model for calculating heat fluxes due to the Redi diffusivity. The last two terms in (15) result from the off-diagonal terms of $\mathbf{K}$ and are not positive-definite. Griffies et al. (1998) present a physical interpretation of χ_e in (15) as comprising two components. The first component is an isotropic diffusion in all directions that always *decreases* tracer variance and *increases* χ_e—these are the first three terms in (15). The second component is an alignment term that represents the action of isopycnal diffusion to align tracer contours with the neutral direction—these are the last two terms in (15). This second component *increases* tracer variance and *decreases* χ_e as structure is added to the tracer field. They show that the *global* integral of χ_e is guaranteed to be positive. Thus, a Redi diffusivity is guaranteed to decrease the tracer variance globally but is not guaranteed to do so locally since the alignment term is not guaranteed to be positive-definite. However, we find that $\chi_e > 0$ for the ECCO estimate when averaged over the NATRE region and proceed with interpreting the mean profile of χ_e and K_e.

The ECCO adjustment process begins with a first guess for K_e specified as a constant value of 1000 m² s⁻¹. The adjusted K_e has significant vertical structure; it is large in the top 500 m and below 2000 m, where gradients are quite weak (Fig. 5a). A middepth increase is seen between 800 and 1500 m, exactly where $|\nabla_\rho^h T|$ and the microstructure residual estimate of χ_e peak. Given the χ_e profile in Fig. 5c, we suggest the following interpretation. Below 1500 m, K_e strongly increases with depth while χ_e strongly decreases in a manner similar to the POP 1/10° simulation and the microstructure residual. Forget et al. (2015b) show that the adjusted coefficients significantly improve the simulation of the oxygen field at depth, reminiscent of the CESM2 usage of enhanced K_e at depth to improve the representation of passive tracers (Danabasoglu et al. 2020). Since $|\nabla_\rho^h T|$ is quite small below 2000 m, an artificially enhanced K_e at these depths would not degrade the temperature field. Forget et al. (2015b) write that K_e adjustments are primarily a result of adjusting to fit the Argo observations. Given that inference, the disagreement between the middepth peak in adjusted K_e and the Cole et al. (2015) estimate of K_e

is intriguing. Fundamentally, the information used for both is the same: along-isopycnal anomalies of salinity as measured by Argo floats, but that information is interpreted using different models and different inversion procedures to yield two qualitative different profiles of K_e. We also note that none of the other estimates of K_e in the region indicate a middepth peak (see Groeskamp et al. 2020b, their Fig. 1). We then suggest interpreting the middepth peak in adjusted K_e as a sign that the adjustments in the 1000–1500-m range are compensating for a different deficiency in simulating $|\nabla_\rho^h T|$, while helping minimize the overall misfit to Argo observations.

6. Discussion

We presented a novel attempt at analyzing the representation of mesoscale eddy stirring in production configurations of ocean general circulation models through a comparison against Ferrari and Polzin (2005)'s interpretation of the NATRE microstructure data (section 4a). Framing the discussion of mesoscale stirring in terms of χ, the rate of dissipation of temperature variance, provides an interesting view on observational estimates and model parameterizations of along-isopycnal eddy diffusivity K_e. For the NATRE region, we find that the variance dissipated in the CESM-H POP2 1/10° simulation analyzed by Guo et al. (2022) agrees very well with an estimate of χ_e derived from the Ferrari and Polzin (2005) microstructure analysis (section 4b). Applying a similar framework to a 1° CESM-L POP2 simulation with parameterized mesoscale diffusivity paints the model as being unable to maintain the isopycnal water mass contrast between the Mediterranean outflow and ambient waters, upstream of the NATRE region (section 5b). Analysis of the ECCOV4r4 state estimate with K_e adjusted to minimize misfit of the solution suggests caution in interpreting the adjusted K_e as indicative of physical processes (section 5c).

Strong inferences are lacking. For one, the method relies on the opportunistic use of temperature as a passive tracer, and so is limited to regions of large-scale T–S compensation (spiciness). Second, the method requires a large number of microstructure measurements, distributed over a large area. The NATRE (Ferrari and Polzin 2005) and DIMES (Naveira Garabato et al. 2016) datasets are unique in this regard, but ultimately represent a small part of the ocean. Even then, the error bars are quite large and prevent concrete quantitative insights at the moment. The above considerations imply that a direct model–data comparison, as demonstrated here, is of limited utility in developing new mesoscale parameterizations or quantitatively judging high-resolution simulations. However, microstructure data collection is increasing rapidly, including on novel platforms such as temperature microstructure measurements on Global Ocean Ship-Based Hydrographic Investigations Program (GO-SHIP) CTD rosettes (Goto et al. 2018), and potentially both shear and temperature microstructure on Argo floats in the future (Roemmich et al. 2019). Expanded collection of microstructure data, analyzed in concert with careful analysis of high-resolution mesoscale-resolving models (e.g., Guo et al. 2022) as presented here, might yield more useful insights in the future. Finally, we suggest that the use of a variance budget framework, and specifically χ_e as a metric,

appears to be a promising way to compare high-resolution and low-resolution ocean models.

Data availability statement. Datasets for terms in Figs. 3 and 4 and the code to reproduce these figures are provided online at https://github.com/dcherian/cherian-2023-eddydiff. The MITgcm modifications to support extra diagnostic output are available at https://github.com/dcherian/MITgcm/tree/chi-diags. Rerunning the simulation should be possible following the instructions in Wang and Fenty (2023). These datasets represent small subsets (time averages over the NATRE region) of large simulations, but should still be useful for comparison purposes. The dataset from Cole et al. (2015) is publicly available at Cole et al. (2018). The datasets from Groeskamp et al. (2020b) are publicly available at Groeskamp et al. (2020a).

REFERENCES

Abernathey, R., A. Gnanadesikan, M.-A. Pradal, and M. A. Sundermeyer, 2022a: Isopycnal mixing. *Ocean Mixing*, Elsevier, 215–256.

Abernathey, R. P., and Coauthors, 2022b: Xgcm, version v0.8.1. Zenodo, accessed 15 February 2022, https://doi.org/10.5281/ZENODO.826925.

Alford, M. H., M. C. Gregg, and E. A. D'Asaro, 2005: Mixing, 3D mapping, and Lagrangian evolution of a thermohaline intrusion. *J. Phys. Oceanogr.*, **35**, 1689–1711, https://doi.org/10.1175/JPO2780.1.

——, J. A. MacKinnon, H. L. Simmons, and J. D. Nash, 2016: Near-inertial internal gravity waves in the ocean. *Annu. Rev. Mar. Sci.*, **8**, 95–123, https://doi.org/10.1146/annurev-marine-010814-015746.

Bachman, S. D., B. Fox-Kemper, and F. O. Bryan, 2015: A tracer-based inversion method for diagnosing eddy-induced diffusivity and advection. *Ocean Modell.*, **86**, 1–14, https://doi.org/10.1016/j.ocemod.2014.11.006.

——, ——, and ——, 2020: A diagnosis of anisotropic eddy diffusion from a high-resolution global ocean model. *J. Adv.*

Model. Earth Syst., **12**, e2019MS001904, https://doi.org/10.1029/2019MS001904.

Boyer, T., and Coauthors, 2018: *World Ocean Atlas 2018*. NOAA Atlas NESDIS.

Bryan, F., and S. Bachman, 2015: Isohaline salinity budget of the North Atlantic salinity maximum. *J. Phys. Oceanogr.*, **45**, 724–736, https://doi.org/10.1175/JPO-D-14-0172.1.

Caswell, T. A., and Coauthors, 2023: Matplotlib. Zenodo, accessed 9 September 2022, https://doi.org/10.5281/ZENODO.592536.

Cole, S. T., C. Wortham, E. Kunze, and W. B. Owens, 2015: Eddy stirring and horizontal diffusivity from Argo float observations: Geographic and depth variability. *Geophys. Res. Lett.*, **42**, 3989–3997, https://doi.org/10.1002/2015GL063827.

——, C. J. L. Wortham, E. Kunze, and W. B. Owens, 2018: Eddy diffusivity from Argo temperature and salinity profiles. Accessed 1 January 2019, https://doi.org/10.1575/1912/10220.

Computational and Information Systems Laboratory, 2019: Cheyenne: SGI ICE XA Cluster (Climate Simulation Laboratory). National Center for Atmospheric Research, https://doi.org/10.5065/D6RX99HX.

Danabasoglu, G., and J. Marshall, 2007: Effects of vertical variations of thickness diffusivity in an ocean general circulation model. *Ocean Modell.*, **18**, 122–141, https://doi.org/10.1016/j.ocemod.2007.03.006.

——, S. C. Bates, B. P. Briegleb, S. R. Jayne, M. Jochum, W. G. Large, S. Peacock, and S. G. Yeager, 2012: The CCSM4 ocean component. *J. Climate*, **25**, 1361–1389, https://doi.org/10.1175/JCLI-D-11-00091.1.

——, and Coauthors, 2020: The Community Earth System Model version 2 (CESM2). *J. Adv. Model. Earth Syst.*, **12**, e2019MS001916, https://doi.org/10.1029/2019MS001916.

Davis, R. E., 1994a: Diapycnal mixing in the ocean: Equations for large-scale budgets. *J. Phys. Oceanogr.*, **24**, 777–800, https://doi.org/10.1175/1520-0485(1994)024<0777:DMITOE>2.0.CO;2.

——, 1994b: Diapycnal mixing in the ocean: The Osborn–Cox model. *J. Phys. Oceanogr.*, **24**, 2560–2576, https://doi.org/10.1175/1520-0485(1994)024<2560:DMITOT>2.0.CO;2.

de La Lama, M. S., J. H. LaCasce, and H. K. Fuhr, 2016: The vertical structure of ocean eddies. *Dyn. Stat. Climate Syst.*, **1**, dzw001, https://doi.org/10.1093/climsys/dzw001.

Elson, P., and Coauthors, 2022: SciTools/cartopy: V0.21.1. Zenodo, accessed 9 September 2022, https://doi.org/10.5281/ZENODO.1182735.

Ferrari, R., and D. L. Rudnick, 2000: Thermohaline variability in the upper ocean. *J. Geophys. Res.*, **105**, 16 857–16 883, https://doi.org/10.1029/2000JC900057.

——, and K. L. Polzin, 2005: Finescale structure of the T-S relation in the eastern North Atlantic. *J. Phys. Oceanogr.*, **35**, 1437–1454, https://doi.org/10.1175/JPO2763.1.

——, and M. Nikurashin, 2010: Suppression of eddy diffusivity across Jets in the Southern Ocean. *J. Phys. Oceanogr.*, **40**, 1501–1519, https://doi.org/10.1175/2010JPO4278.1.

Forget, G., J.-M. Campin, P. Heimbach, C. N. Hill, R. M. Ponte, and C. Wunsch, 2015a: ECCO version 4: An integrated framework for non-linear inverse modeling and global ocean state estimation. *Geosci. Model Dev.*, **8**, 3071–3104, https://doi.org/10.5194/gmd-8-3071-2015.

——, D. Ferreira, and X. Liang, 2015b: On the observability of turbulent transport rates by Argo: Supporting evidence from an inversion experiment. *Ocean Sci.*, **11**, 839–853, https://doi.org/10.5194/os-11-839-2015.

Gargett, A. E., 1989: Ocean turbulence. *Annu. Rev. Fluid Mech.*, **21**, 419–451, https://doi.org/10.1146/annurev.fl.21.010189.002223.

Garrett, C., 2001: Stirring and mixing: What are the rate-controlling processes? *Proc.'Aha Huliko'a Hawaiian Winter Workshop*, Honolulu, HI, University of Hawai'i at Mānoa, 8 pp., https://www.soest.hawaii.edu/PubServices/2001pdfs/Garrett.pdf.

Gent, P. R., J. Willebrand, T. J. McDougall, and J. C. McWilliams, 1995: Parameterizing eddy-induced tracer transports in ocean circulation models. *J. Phys. Oceanogr.*, **25**, 463–474, https://doi.org/10.1175/1520-0485(1995)025<0463:PEITTI>2.0.CO;2.

Gnanadesikan, A., D. Bianchi, and M.-A. Pradal, 2013: Critical role for mesoscale eddy diffusion in supplying oxygen to hypoxic ocean waters. *Geophys. Res. Lett.*, **40**, 5194–5198, https://doi.org/10.1002/grl.50998.

——, M.-A. Pradal, and R. Abernathey, 2015a: Exploring the isopycnal mixing and helium–heat paradoxes in a suite of Earth system models. *Ocean Sci.*, **11**, 591–605, https://doi.org/10.5194/os-11-591-2015.

——, ——, and ——, 2015b: Isopycnal mixing by mesoscale eddies significantly impacts oceanic anthropogenic carbon uptake. *Geophys. Res. Lett.*, **42**, 4249–4255, https://doi.org/10.1002/2015GL064100.

Goto, Y., I. Yasuda, and M. Nagasawa, 2018: Comparison of turbulence intensity from CTD-attached and free-fall microstructure profilers. *J. Atmos. Oceanic Technol.*, **35**, 147–162, https://doi.org/10.1175/JTECH-D-17-0069.1.

Gregg, M. C., 1987: Diapycnal mixing in the thermocline: A review. *J. Geophys. Res.*, **92**, 5249–5286, https://doi.org/10.1029/JC092iC05p05249.

——, D. P. Winkel, T. B. Sanford, and H. Peters, 1996: Turbulence produced by internal waves in the oceanic thermocline at mid and low latitudes. *Dyn. Atmos. Oceans*, **24**, 1–14, https://doi.org/10.1016/0377-0265(95)00406-8.

——, E. A. D'Asaro, J. J. Riley, and E. Kunze, 2018: Mixing efficiency in the ocean. *Annu. Rev. Mar. Sci.*, **10**, 443–473, https://doi.org/10.1146/annurev-marine-121916-063643.

Griffies, S. M., A. Gnanadesikan, R. C. Pacanowski, V. D. Larichev, J. K. Dukowicz, and R. D. Smith, 1998: Isoneutral diffusion in a *z*-coordinate ocean model. *J. Phys. Oceanogr.*, **28**, 805–830, https://doi.org/10.1175/1520-0485(1998)028<0805:IDIAZC>2.0.CO;2.

——, and Coauthors, 2016: OMIP contribution to CMIP6: Experimental and diagnostic protocol for the physical component of the ocean model intercomparison project. *Geosci. Model Dev.*, **9**, 3231–3296, https://doi.org/10.5194/gmd-9-3231-2016.

Groeskamp, S., J. H. LaCasce, T. McDougall, and M. Rogé, 2020a: Mixing diffusivities. figshare, accessed 1 June 2021, https://doi.org/10.6084/m9.figshare.12554555.v2.

——, ——, T. J. McDougall, and M. Rogé, 2020b: Full-depth global estimates of ocean mesoscale eddy mixing from observations and theory. *Geophys. Res. Lett.*, **47**, e2020GL089425, https://doi.org/10.1029/2020GL089425.

Guo, Y., S. Bishop, F. Bryan, and S. Bachman, 2022: A global diagnosis of eddy potential energy budget in an eddy-permitting ocean model. *J. Phys. Oceanogr.*, **52**, 1731–1748, https://doi.org/10.1175/JPO-D-22-0029.1.

Hoyer, S., and J. Hamman, 2017: Xarray: N-D labeled arrays and datasets in Python. *J. Open Res. Software*, **5**, 10, https://doi.org/10.5334/jors.148.

——, and Coauthors, 2023: Xarray. Zenodo, accessed 1 September 2023, https://doi.org/10.5281/ZENODO.598201.

Hunter, J. D., 2007: Matplotlib: A 2D graphics environment. *Comput. Sci. Eng.*, **9**, 90–95, https://doi.org/10.1109/MCSE.2007.55.

Jackson, L., R. Hallberg, and S. Legg, 2008: A parameterization of shear-driven turbulence for ocean climate models. *J. Phys. Oceanogr.*, **38**, 1033–1053, https://doi.org/10.1175/2007JPO3779.1.

Klocker, A., and R. Abernathey, 2014: Global patterns of mesoscale eddy properties and diffusivities. *J. Phys. Oceanogr.*, **44**, 1030–1046, https://doi.org/10.1175/JPO-D-13-0159.1.

——, R. Ferrari, and J. H. LaCasce, 2012: Estimating suppression of eddy mixing by mean flows. *J. Phys. Oceanogr.*, **42**, 1566–1576, https://doi.org/10.1175/JPO-D-11-0205.1.

Kunze, E., 2017: Internal-wave-driven mixing: Global geography and budgets. *J. Phys. Oceanogr.*, **47**, 1325–1345, https://doi.org/10.1175/JPO-D-16-0141.1.

——, E. Firing, J. M. Hummon, T. K. Chereskin, and A. M. Thurnherr, 2006: Global abyssal mixing inferred from lowered ADCP shear and CTD strain profiles. *J. Phys. Oceanogr.*, **36**, 1553–1576, https://doi.org/10.1175/JPO2926.1.

LaCasce, J. H., 2017: The prevalence of oceanic surface modes. *Geophys. Res. Lett.*, **44**, 11 097–11 105, https://doi.org/10.1002/2017GL075430.

——, and S. Groeskamp, 2020: Baroclinic modes over rough bathymetry and the surface deformation radius. *J. Phys. Oceanogr.*, **50**, 2835–2847, https://doi.org/10.1175/JPO-D-20-0055.1.

Large, W. G., and P. R. Gent, 1999: Validation of vertical mixing in an equatorial ocean model using large eddy simulations and observations. *J. Phys. Oceanogr.*, **29**, 449–464, https://doi.org/10.1175/1520-0485(1999)029<0449:VOVMIA>2.0.CO;2.

——, J. C. McWilliams, and S. C. Doney, 1994: Oceanic vertical mixing: A review and a model with a nonlocal boundary layer parameterization. *Rev. Geophys.*, **32**, 363–403, https://doi.org/10.1029/94RG01872.

Ledwell, J. R., A. J. Watson, and C. S. Law, 1998: Mixing of a tracer in the pycnocline. *J. Geophys. Res.*, **103**, 21 499–21 529, https://doi.org/10.1029/98JC01738.

MacKinnon, J. A., and Coauthors, 2017: Climate process team on internal wave-driven ocean mixing. *Bull. Amer. Meteor. Soc.*, **98**, 2429–2454, https://doi.org/10.1175/BAMS-D-16-0030.1.

Menemenlis, D., J.-M. Campin, P. Heimbach, C. Hill, T. Lee, A. Nguyen, M. Schodlok, and H. Zhang, 2008: ECCO2: High resolution global ocean and sea ice data synthesis. *Mercator Ocean Quarterly Newsletter*, No. 31, Mercator Ocean International, Toulouse, France, 13–21, https://www.mercator-ocean.eu/wp-content/uploads/2015/06/lettre_31_en.pdf.

Met Office, 2010: Cartopy: A cartographic Python library with a Matplotlib interface. Met Office, https://www.bibsonomy.org/bibtex/2bc7d5c53e98cbff7a56b008bb2ce170c/pbett.

MITgcm Group, 2023: MITgcm user manual. https://mitgcm.readthedocs.io/en/latest/.

Munk, W. H., 1966: Abyssal recipes. *Deep-Sea Res. Oceanogr. Abstr.*, **13**, 707–730, https://doi.org/10.1016/0011-7471(66)90602-4.

Naveira Garabato, A. C., K. L. Polzin, R. Ferrari, J. D. Zika, and A. Forryan, 2016: A microscale view of mixing and overturning across the Antarctic Circumpolar Current. *J. Phys. Oceanogr.*, **46**, 233–254, https://doi.org/10.1175/JPO-D-15-0025.1.

Osborn, T. R., 1980: Estimates of the local rate of vertical diffusion from dissipation measurements. *J. Phys. Oceanogr.*, **10**, 83–89, https://doi.org/10.1175/1520-0485(1980)010<0083:EOTLRO>2.0.CO;2.

——, and C. S. Cox, 1972: Oceanic fine structure. *Geophys. Fluid Dyn.*, **3**, 321–345, https://doi.org/10.1080/03091927208236085.

Redi, M. H., 1982: Oceanic isopycnal mixing by coordinate rotation. *J. Phys. Oceanogr.*, **12**, 1154–1158, https://doi.org/10.1175/1520-0485(1982)012<1154:OIMBCR>2.0.CO;2.

Reichl, B. G., and R. Hallberg, 2018: A simplified energetics based Planetary Boundary Layer (ePBL) approach for ocean climate simulations. *Ocean Modell.*, **132**, 112–129, https://doi.org/10.1016/j.ocemod.2018.10.004.

Roemmich, D., and J. Gilson, 2009: The 2004–2008 mean and annual cycle of temperature, salinity, and steric height in the global ocean from the Argo Program. *Prog. Oceanogr.*, **82**, 81–100, https://doi.org/10.1016/j.pocean.2009.03.004.

——, and Coauthors, 2019: On the future of Argo: A global, full-depth, multi-disciplinary array. *Front. Mar. Sci.*, **6**, 439, https://doi.org/10.3389/fmars.2019.00439.

Schmit, R. W., J. M. Toole, R. L. Koehler, E. C. Mellinger, and K. W. Doherty, 1988: The development of a fine- and microstructure profiler. *J. Atmos. Oceanic Technol.*, **5**, 484–500, https://doi.org/10.1175/1520-0426(1988)005<0484:TDOAFA>2.0.CO;2.

Smith, K. S., and R. Ferrari, 2009: The production and dissipation of compensated thermohaline variance by mesoscale stirring. *J. Phys. Oceanogr.*, **39**, 2477–2501, https://doi.org/10.1175/2009JPO4103.1.

Smith, R., and Coauthors, 2010: The Parallel Ocean Program (POP) reference manual. Tech. Rep. LAUR-10-01853, 141 pp., https://www2.cesm.ucar.edu/models/cesm1.0/pop2/doc/sci/POPRefManual.pdf.

Spingys, C. P., A. C. Naveira Garabato, S. Legg, K. L. Polzin, E. P. Abrahamsen, C. E. Buckingham, A. Forryan, and E. E. Frajka-Williams, 2021: Mixing and transformation in a deep western boundary current: A case study. *J. Phys. Oceanogr.*, **51**, 1205–1222, https://doi.org/10.1175/JPO-D-20-0132.1.

St. Laurent, L., and R. W. Schmitt, 1999: The contribution of salt fingers to vertical mixing in the North Atlantic tracer release experiment. *J. Phys. Oceanogr.*, **29**, 1404–1424, https://doi.org/10.1175/1520-0485(1999)029<1404:TCOSFT>2.0.CO;2.

Tsujino, H., and Coauthors, 2018: JRA-55 based surface dataset for driving ocean–sea-ice models (JRA55-do). *Ocean Modell.*, **130**, 79–139, https://doi.org/10.1016/j.ocemod.2018.07.002.

Umlauf, L., and H. Burchard, 2003: A generic length-scale equation for geophysical turbulence models. *J. Mar. Res.*, **61**, 235–265.

Wang, O., and I. Fenty, 2023: Instructions for reproducing ECCO version 4 release 4. Zenodo, 8 pp., https://doi.org/10.5281/ZENODO.7839058.

Waterhouse, A. F., and Coauthors, 2014: Global patterns of diapycnal mixing from measurements of the turbulent dissipation rate. *J. Phys. Oceanogr.*, **44**, 1854–1872, https://doi.org/10.1175/JPO-D-13-0104.1.

Whalen, C. B., J. A. MacKinnon, L. D. Talley, and A. F. Waterhouse, 2015: Estimating the mean diapycnal mixing using a finescale strain parameterization. *J. Phys. Oceanogr.*, **45**, 1174–1188, https://doi.org/10.1175/JPO-D-14-0167.1.

——, ——, and ——, 2018: Large-scale impacts of the mesoscale environment on mixing from wind-driven internal waves. *Nat. Geosci.*, **11**, 842–847, https://doi.org/10.1038/s41561-018-0213-6.

Wunsch, C., 1999: Where do ocean eddy heat fluxes matter? *J. Geophys. Res.*, **104**, 13 235–13 249, https://doi.org/10.1029/1999JC900062.